Self-Assembled Synthesis of Mesocrystalline TiO$_2$@C-rGO Hybrid Nanostructures for Highly Reversible Sodium Storage

Zhensheng Hong,*[,†,‡] Kaiqiang Zhou,[†,‡] Junwen Zhang,[†,§] Zhigao Huang,[†,‡] and Mingdeng Wei*[,⊥]

[†]Fujian Provincial Key Laboratory of Quantum Manipulation and New Energy Materials, College of Physics and Energy, Fujian Normal University, Fuzhou, Fujian 350117, China

[‡]Fujian Provincial Collaborative Innovation Center for Optoelectronic Semiconductors and Efficient Devices, Xiamen 361005, China

[§]Shenzhen Key Laboratory of Transformation Optics and Spatial Modulation, Kuang-Chi Institute of Advanced Technology, Shenzhen, Guangdong 518057, China

[⊥]State Key Laboratory of Photocatalysis on Energy and Environment, Fuzhou University, Fuzhou, Fujian 350002, China

Ⓢ *Supporting Information*

ABSTRACT: With the aim of enhancing the electrochemical kinetics and capacity of the TiO$_2$ electrode for Na ion batteries (NIBs), we have designed a hybrid material of carbon-coated TiO$_2$ mesocrystals anchored on reduced graphene oxide (TiO$_2$@C-rGO). Such hybrid nanostructures are fabricated through a facile one-step route including in situ growth of oriented self-assembly of TiO$_2$ mesocrystals on GO. TiO$_2$@C-rGO possesses a very large surface area (279 m^2 g^{-1}), mesoporous nature, and single-crystal-like structure. It is also found that the capacity of TiO$_2$ electrode for NIBs could be improved by carbon coating at a low current rate, but pure TiO$_2$ shows better rate performance than that of TiO$_2$@C. Remarkably, the enhanced electrochemical kinetics and large capacity can be simultaneously achieved by designing hybrid material. The hybrid nanostructures exhibit a highly reversible capacity of 300 mAh g^{-1} at 100 mA g^{-1}, superior rate capability, and long-term cycling stability (a stable capacity of 159 mAh g^{-1} can be maintained after 1000 cycles at 1 A g^{-1}). The superior Na ion storage of TiO$_2$@C-rGO is largely ascribed to the robust architecture of well-dispersed carbon-coated mesoporous TiO$_2$ mesocrystals anchored on conductive graphene network, leading to enhanced electrochemical kinetics and offering enough active sites for the Na ion to locate.
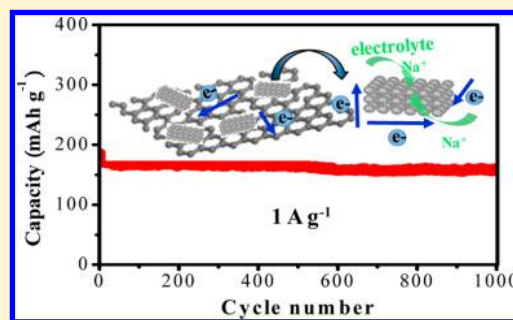
1. INTRODUCTION

Development of rechargeable batteries is significantly important to realize applications of portable electronics, electric vehicles (EVs), and stationary energy storage. Lithium ion batteries (LIBs) remain the most prominent battery technology compared to other secondary battery systems due to the high energy density and long cycle life.[1,2] However, there is an increasing awareness and worry about the cost and the limitation of lithium reserves in the large-scale applications of LIBs.[3] Recently, Na ion batteries (NIBs) with identical conception have received much attention because Na is cheap and abundant, the second lightest and more evenly distributed alkali metal element compared to Li.[3−7] However, NIBs suffered from low electrochemical reaction kinetics because of the larger diameter of the Na ion (0.97 Å) compared to Li ion (0.68 Å), which makes it difficult to find available electrode materials for Na ion storage.[8] In particular, developing suitable anode (negative) materials for Na ion storage is still a major obstacle in realizing NIBs.[5,6]

Up to now, many efforts have been devoted to investigate anode materials for NIBs. Hard carbons as negative materials for NIBs have been reported in previous studies; however, these delivered limited capacity at high current rate.[9,10] It has

been demonstrated that the Na ion can insert and extract into a graphite host through co-intercalation with solvent, which showed a reversible capacity of only ca. 100 mAh g^{-1}.[11,12] Similar to LIBs, alloy-type (Sn and Sb)[13,14] and conversion-type mechanism (Co$_3$O$_4$, CuO, and MoS$_2$) anode materials[15−17] display high initial capacity for Na ion storage, but many of them have suffered from poor cycling stability due to the large volume change. Classical insertion materials such as Na$_2$Ti$_3$O$_7$ can deliver an initial capacity of more than 200 mAh g^{-1}; however, such a material so far has not shown satisfactory cycling stability.[18] Some novel titanate compounds were also investigated as anodes for NIBs, which remain relatively unexplored.[19−21]

Recently, nanostructured TiO$_2$ has exhibited promising applications in NIBs, which delivered acceptable capacity and good cycling performance.[22−31] In general, the electrochemical properties of TiO$_2$ including the capacity are greatly affected by microstructures. Many strategies have been adopted to synthesize TiO$_2$ nanostructures with various morphologies,

such as nanorods, nanotubes, nanosheets, hollow sphere/nanobox, mesoporous structures, and mesocrystals.[24,25,28−36] Among them, crystallographically oriented nanoparticle superstructures (mesocrystals) have attracted great interest in applications for energy storage and conversion.[32−35] Mesocrystals, built by individual nanocrystal subunits with crystallographically oriented directions, are usually formed through an oriented self-assembly process. Mesocrystals have been demonstrated to significantly enhance the capacity and rate performance in LIBs and NIBs.[28,29,32−34]

Beyond considering the morphology of TiO_2, many efforts have been carried out developing composite materials, which usually were composed of TiO_2 and other conductive phases. Pure TiO_2 suffers from intrinsically poor electronic conductivity, which can be overcome by incorporation of conductive materials with pristine TiO_2. Carbon coatings are known to be a promising route to improve the electrochemical performance of various electrode materials. It is also demonstrated that carbon-coated anatase TiO_2 exhibited improved Na ion storage performance.[22,25,26,37] Compared to carbons, graphene sheets, atomic layers of graphitic carbons, exhibit some unique advantages such as excellent electrical conductivity, large surface area, and structural flexibility.[38,39] The aggregation of the nanoparticles can be effectively inhibited when the GO is used as a substrate for nanoparticles to scatter. These features render graphene sheets an attractive material for fabricating hybrid electrode materials with enhanced electrochemical properties.[23,24,39−41]

In this study, we design a hybrid material of carbon-coated mesoporous TiO_2 mesocrystals anchored on reduced graphene oxide (TiO_2@C-rGO) as an anode material for NIBs. Such hybrid nanostructures were fabricated through a facile one-step route including in situ growth of oriented self-assembly of TiO_2 mesocrystals on graphene oxide. The hybrid nanostructures exhibited a highly reversible capacity of 300 mAh g^{-1} at 100 mA g^{-1}, superior rate capability, and long-term cycling stability for Na ion storage.

2. EXPERIMENTAL SECTION

2.1. Materials Synthesis. We developed a facile route to form hybrid nanostructures of carbon-coated mesoporous TiO_2 mesocrystals anchored on reduced graphene oxide (denoted as TiO_2@C-rGO) sheets. Graphene oxide (GO) sheets were prepared through a well-known modified Hummers method, also used by our previous report.[41] First, 0.5 g polyvinylpyrrolidone (PVP) and 30 mg of GO sheets were dissolved and dispersed into 50 mL 2.1 M HNO_3 solution under sonication. Then, 2 g sodium dodecyl sulfate (SDS) was first dissolved into the solution. After stirring for a few minutes, 1 mL titanium(IV) isopropoxide (TIP) was added into the obove solution and kept at 70 °C for 48 h under stirring. The sample was obtained by centrifugation, washed thoroughly with distilled water and ethanol, and dried at 60 °C overnight. Finally, TiO_2@C-rGO was harvested by calcining at 400 °C for 120 min and then 600 °C for 180 min under Ar flow. Carbon-coated TiO_2 mesocrystals (TiO_2@C) were synthesized under the same reaction condition without the presence of GO. As a reference, pure TiO_2 mesocrystals were obtained by calcining at 400 °C for 120 min in air to remove the residual organics. The chemicals with analytical grade were purchased from Aladdin Company without further purification.

2.2. Characterization of the Samples. Scanning electron microscopy (SEM, S8010 instrument) and transmission electron microscopy (TEM, FEI F20 S-TWIN instrument) were applied for the morphological and structural characterization of the samples. X-ray diffraction (XRD) patterns were recorded on a Rigaku Ultima IV diffractometer, using Ni filtered Cu Ka radiation (λ = 1.5406 Å). N_2 adsorption−desorption analysis was measured on a Micromeritics TriStar II 3020 instrument (USA). Pore size distribution plot was obtained by the Barrett−Joyner−Halenda (BJH) method. The Raman spectra were recorded on a LabRAM HR Evolution (HORIBA Jobin Yvon) with a 532 nm laser.

2.3. Electrochemical Measurements. For the electrochemical measurement of Na ion intercalation, the active materials (pure TiO_2, TiO_2@C, and TiO_2@C-rGO) were admixed with super-P and polyvinylidene fluoride (PVDF) binder additive in a weight ratio of 80:10:10. It is noted that the calculated capacity is based on the total active weight of TiO_2@C and TiO_2@C-rGO. The mixture was pressed on copper foil circular flakes as working electrodes (WE), and dried at 120 °C in vacuum for 12 h. Na ion cells were assembled in coin-type cells (CR 2025) with a Na metal foil as the negative electrode, glass fiber separator (Whatman GF/F), and 1 M $NaClO_4$ in ethylene carbonate (EC) and diethyl carbonate (DEC) (1/1 in volume) as the electrolyte. The mass loading of active material in the electrode was around 1.2 mg cm^{-2}, and the amount of electrolyte was 170−200 μL. The cells were fabricated in a glovebox filled with highly pure argon gas (O_2 and H_2O levels <1 ppm), and charge/discharge profiles were tested in the voltage range of 0.01 to 3.0 V (Na$^+$/Na) on a Land automatic battery tester (Land CT 2001A, Wuhan, China). Cyclic voltammetry (CV) measurements were performed on Zennium (Zahner). Electrochemical impedance spectroscopy (EIS) was also conducted on Zennium electrochemical workstation with an AC voltage amplitude of 5 mV in the frequency range from 1 MHz to 100 mHz.

3. RESULTS AND DISCUSSION

The hybrid nanostructures of carbon-coated mesoporous TiO_2 mesocrystals on reduced graphene oxide (TiO_2@C-rGO) were synthesized through a facile wet chemical and in situ synthesis route under the assistance of surfactants. As shown in Figure 1,

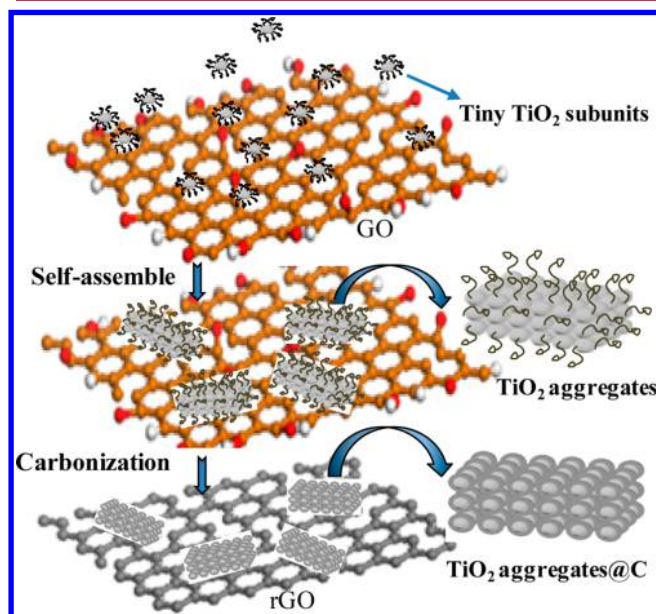**Figure 1.** Schematic illustration of the formation of TiO_2@C-rGO.

GO sheets were dispersed into HNO_3 solution with the presence of PVP, and then the tiny TiO_2 subunits formed from the hydrolysis of YBT (titanium isopropoxide) were temporarily stabilized by surfactant, which self-assembled into TiO_2 aggregates loaded onto GO sheets. TiO_2@C-rGO were formed by redox reaction and carbonation of GO sheets and organics after thermal treatment. As a reference, TiO_2@C was synthesized without the presence of GO and pure TiO_2
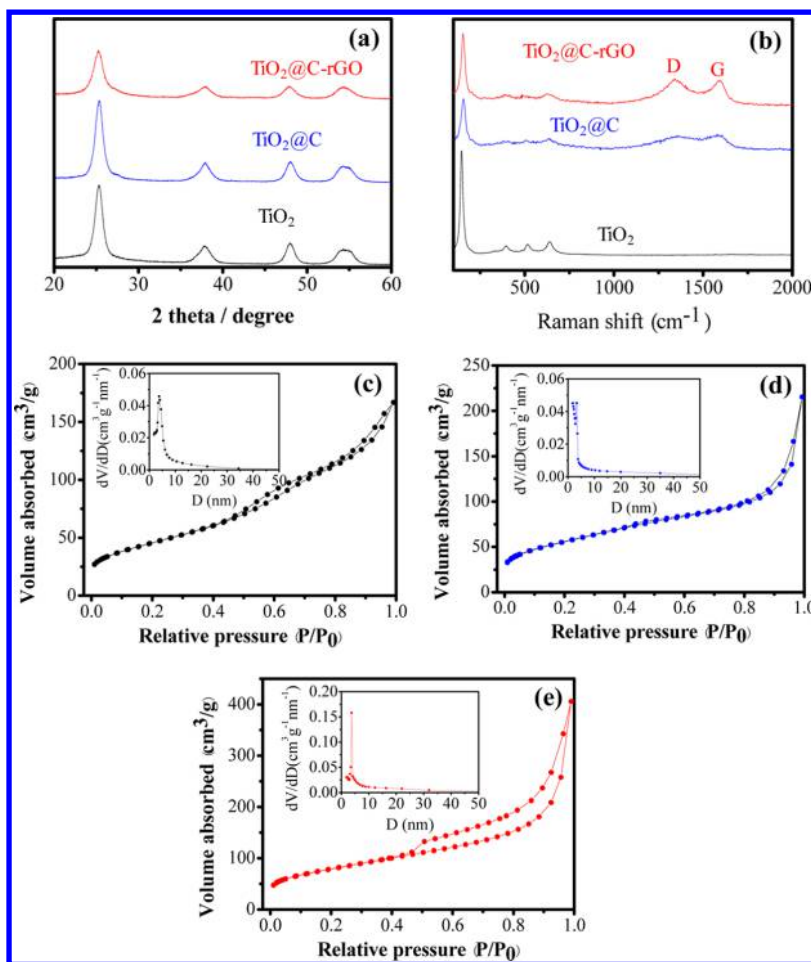
Figure 2. (a) XRD patterns of pure TiO_2, TiO_2@C, and TiO_2@C-rGO. (b) Raman spectra of TiO_2@C and TiO_2@C-rGO. N_2 adsorption−desorption isotherms of (c) pure TiO_2, (d) TiO_2@C, and (e)TiO_2@C-rGO. The insets in (c), (d), and (e) are the corresponding BJH pore size distribution.

mesocrystals were obtained by calcining in air. Figure 2a shows the X-ray diffraction (XRD) patterns of as-prepared samples. All the diffraction peaks in Figure 2a could be exclusively ascribed to tetragonal anatase TiO_2 (JCPDS 04−0477). The broadened diffraction peaks suggest a small crystallite size of the samples. The three samples have similar average crystallite size of approximately 10 nm, using the Scherer equation, based on the (101) diffraction peak. However, TiO_2@C-rGO exhibits lower intensity of the XRD diffraction peaks than the other two samples, which may be due to the hybrid of graphene. Figure 2b shows the Raman spectra of the as prepared TiO_2, TiO_2@C, and TiO_2@C-rGO. A sharp Raman scattering peak was observed at 151 cm^{-1} for the three samples, corresponding to the Eg vibration modes of anatase TiO_2. A couple of peaks at 1326 and 1578 cm^{-1} were assigned to the D-band and G-band of nanocarbon-based materials, respectively. Actually, this is induced by the point defects from the damaged graphene sheets, which is typical for the disordered graphene.[42] The much more intensive scattering peaks of them for TiO_2@C-rGO prove that it has larger content of carbon compared with TiO_2@C. TG curves (Figure S1) revealed that the content of carbon in TiO_2@C and TiO_2@C-rGO was about 8% and 24%, respectively. Therefore, the content of rGO is about 16% in TiO_2@C-rGO.

N_2 adsorption−desorption isotherm measurements were employed to investigate the Brunauer−Emmett−Teller

(BET) surface area and pore size distribution, as presented in Figure 2c−e. The BET surface area and the pore volume of pure TiO_2 were determined to be 163 m^2 g^{-1} and 0.26 cm^3 g^{-1}, respectively. As depicted in Figure 2c (inset), pure TiO_2 exhibits relatively ordered nanopores mainly located around 4.0 nm analyzed using BJH methods. The surface area (198 m^2 g^{-1}) and pore volume (0.32 cm^3 g^{-1}) of TiO_2@C (Figure 2d) are larger than those of pure TiO_2, which could be due to the presence of carbon. As to TiO_2@C-rGO (Figure 2e), the surface area (279 m^2 g^{-1}) and pore volume (0.63 cm^3 g^{-1}) of this hybrid nanostructure are largest among the three samples, which can be due to the remarkable contribution of reduced graphene oxide. The pore size of TiO_2@C is mostly located below 3.3 nm, while TiO_2@C-rGO exhibits a narrow size distribution of mesopores (aroud 3.7 nm).

The morphology of TiO_2@C was characterized by scanning electron microscopy (SEM) and transmission electron microscopy (TEM), and the results are shown in Figure 3. It is observed from the SEM images (Figure 3a,b) that numerous nanoparticles with size of 40−60 nm were formed. Such nanoparticles have a rough surface and porous structure; actually, they are composed of tiny nanoparticle subunits which could be further confirmed by TEM image (Figure 3c). Figure 3d displays HRTEM image of TiO_2@C; the TiO_2 nanocrystal subunits (around 4−5 nm) were highly crystallized, and the clear lattice fringe of 0.35 nm was assigned to the (101) spacing
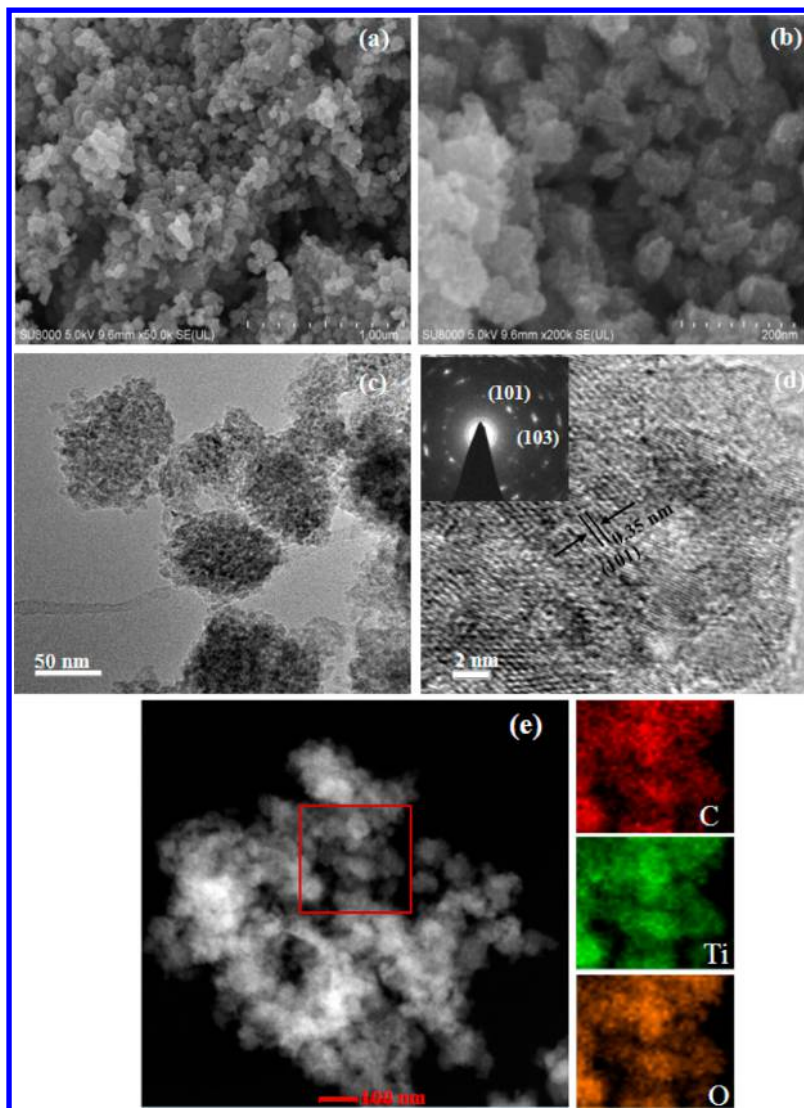
Figure 3. SEM (a,b), TEM (c), and HRTEM (d) and images of TiO$_2$@C. (e) Corresponding EDX elemental mapping C, Ti, and O. The inset in (d) is the related SAED pattern from the whole nanoparticle.

of anatase structure. The corresponding SAED pattern in the inset of Figure 2d for the whole nanoparticle exhibited single-crystal-like diffraction spots, indicating that the building of tiny nanocrystal subunits was highly ordered, thus resulting in the formation of crystallographically oriented mesocrystalline structure. Nevertheless, the diffraction spots were elongated, suggesting that there were some mismatches between the boundaries of the nanoparticle subunits; this is usually found for the mesocrystals which were formed from oriented attachment.[33,35] Furthermore, mesocrystalline TiO$_2$ coated by amorphous carbon could also be observed from the HRTEM image. As shown in Figure 3e, elemental mapping has been carried on the elemental distribution of C, Ti, and O in the composites, verifying that TiO$_2$ mesocrystals were uniformly coated by carbon. The morphology and structure of pure TiO$_2$ were also revealed by SEM, TEM imaging, and SAED patterns; the results are shown in Figure S2. The pure TiO$_2$ with mesoporous and mesocrystalline structure was verified from these characterizations, but they tended to aggregate together.

As depicted by Figure 4a, GO sheets tended to be in an agglomerate state. In this in situ synthesis process of TiO$_2$@C-rGO, GO sheets gradually unfolded during the TiO$_2$ attach-ment; more detailed SEM images are shown in Figure S3. This similar phenomenon was also found in the previous study.[40] Figure 4b,c shows the SEM images of TiO$_2$@C-rGO. The TiO$_2$ nanoparticles were well dispersed and anchored on rGO sheets. TEM image in Figure 4d further confirm and reveal this morphology. Figure 4e displays a single TiO$_2$ nanoparticle loaded on rGO sheets; it also has a mesoporous structure and was constructed by tiny nanocrystal subunits. The correspond-ing SAED pattern from the whole nanoparticle exhibited single-crystal-like diffraction spots, suggesting a crystallographically oriented mesocrystalline structure. Such a structure was further verified by HRTEM image (Figure 4f); all the TiO$_2$ nanocrystal subunits were oriented along the [101] direction. Moreover, it can also be observed that the TiO$_2$ mesocrystals coated by carbon were anchored on reduced graphene oxide. This result was also proved by elemental mapping of C, Ti, and O in the composites, as presented in Figure S4. In addition, PVP has a significant impact on the synthesis of uniform hybrid nanostructures. As shown in Figure S5, many TiO$_2$ nano-particles were not anchored on rGO sheets without the presence of PVP. On the other hand, monodisperse TiO$_2$ nanoparticle with mesocrystalline structure cannot be formed
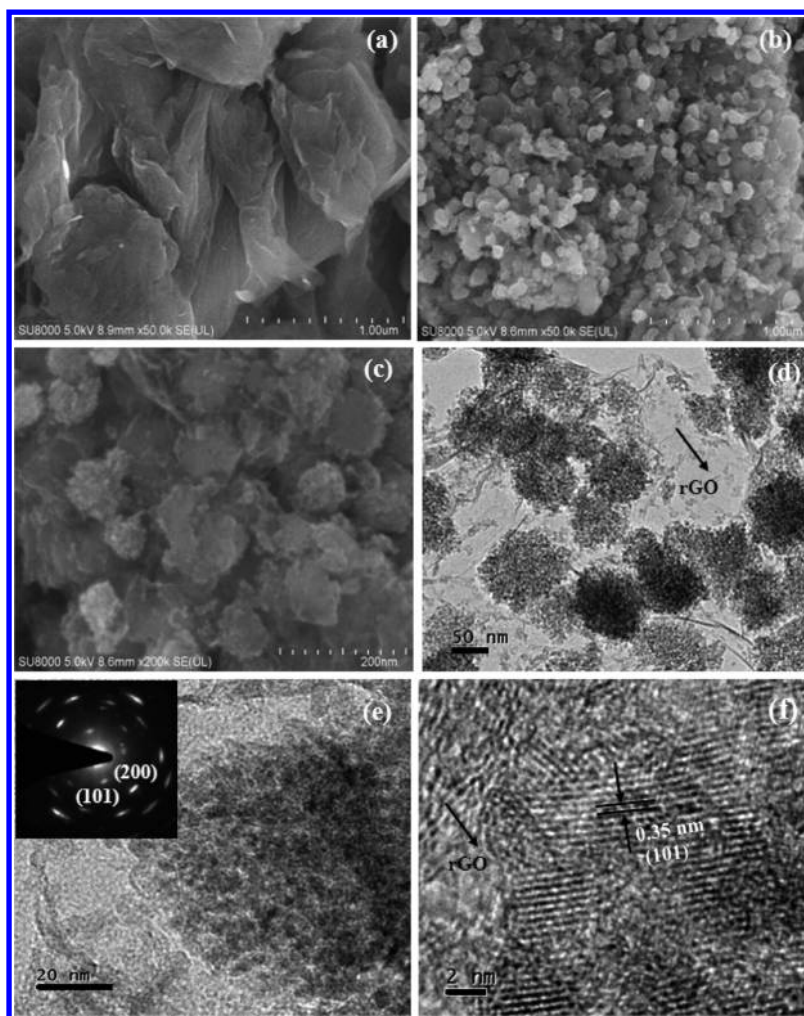
Figure 4. SEM image of GO (a), SEM (b,c), TEM (d,e), and HRTEM (f) and images of TiO_2@C-rGO. The inset in (c) is the related SAED pattern from the whole nanoparticle.

under excess PVP. Similar results were also reported on the synthesis of other GO-based hybrid materials.[43,44]

Recently, a great deal of effort has been devoted to engineering the morphology or designing hybrid materials of TiO_2-based nanostructures to improve their electrochemical storage properties.[23,24,39−41] Herein, we developed hybrid nanostructures of carbon-coated mesoporous TiO_2 mesocrystals anchored on reduced graphene oxide sheets (TiO_2@C-rGO), which would be the expected electrode material with good performance. Cyclic voltammetry (CV) was used for detecting the electrochemical reaction mechanism of the electrode. As depicted in Figure 5a, a couple of redox peaks between 0.5 and 1.0 V vs Na/Na$^+$ with a scan rate of 0.5 mV s^{-1} are observed, probably corresponding to the reversible reduction of Ti^{4+} to Ti^{3+}.[22−29] The irreversible side reactions with electrolyte at the first reduced process were found from the CV measurements. Nevertheless, the redox peaks almost exhibit the same current intensity during the subsequent cycles, indicating a reversible Na ion storage process. Figure 5b shows the charge−discharge profiles of TiO_2@C-rGO from the selective cycles at 0.1 Ag^{1-} in the voltage window of 0.01−3 V. Well-defined voltage plateaus during the charge or discharge process are not observed, which is typical for the anatase TiO_2 anode for Na ion storage. It is notable that TiO_2@C-rGO displays a large discharge capacity of 670 mAh g^{-1} and charge

capacity of 302 mAh g^{-1}. Thus, the reversible capacity of the hybrid nanostructures is much higher than that of other related materials.[22,25−27] Such a relatively larger irreversible capacity is consistent with the CV results. It is founded in the previous report that TiO_2-based anode materials for NIBs displayed low first Coulombic efficiency. This large irreversible capacity could be mainly due to occurrence of a solid−electrolyte interface (SEI) formation and/or a decomposition reaction in active material.[25−28] Pure TiO_2 and TiO_2@C also have similar charge−discharge profiles; the reversible capacities of 201 and 252 mAh g^{-1}, respectively, were obtained at the first cycle. Therefore, the capacity for Na ion storage of TiO_2 mesocrystals could be improved by carbon coating. Moreover, the reversible capacity of the hybrid nanostructures of carbon-coated TiO_2 mesocrystals on reduced graphene oxide (TiO_2@C-rGO) is the largest among them. In addition, the reversible capacity of rGO is about 200 mAh g^{-1} at 100 mA g^{-1} (Figure S7). Thus, the capacity from the rGO is about 32 mAh g^{-1}. The highly reversible capacity of this composite electrode is mainly due to the synergistic effect of intrinsic hybrid nanostructures, which possess a large surface area and well-dispersed morphology, providing enough active sites for Na ion to locate.

Figure 5c presents the rate capability of pure TiO_2, TiO_2@C, and TiO_2@C-rGO from 0.1 to 2 A g^{-1}. The average reversible capacity of TiO_2@C is 230 mAh g^{-1} at 0.1 A g^{-1} (170 mAh g^{-1}

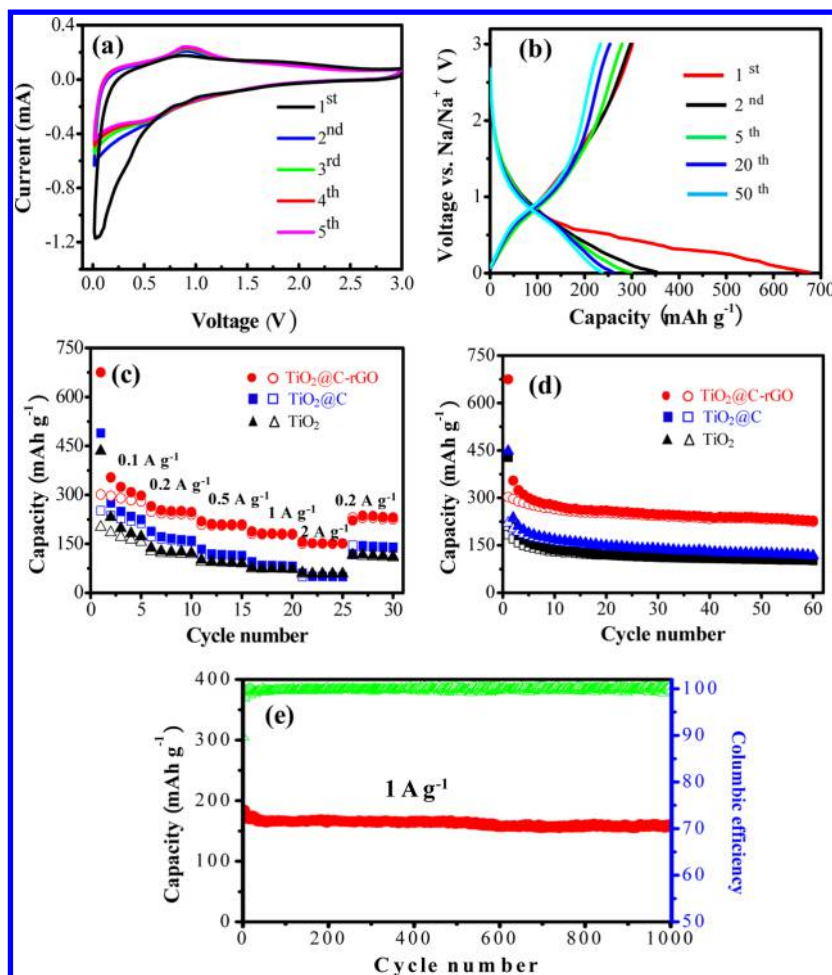**Figure 5.** (a) CV curves of TiO$_2$@C-rGO between 0.01 and 3.0 V with a scan rate of 0.5 mV s^{-1}. (b) Charge−discharge profiles of TiO$_2$@C-rGO at 0.1 A g^{-1}. (c) Rate capability and (d) cycling performance at 0.1 A g^{-1} of pure TiO$_2$, TiO$_2$@C, and TiO$_2$@C-rGO. (e) Long cycling performance of TiO$_2$@C-rGO at 1 A g^{-1}. (filled symbols, discharge capacity; and open symbols, charge capacity)

for pure TiO$_2$) and 51 mAh g^{-1} at a relatively high rate of 2 A g^{-1} (58 mAh g^{-1} for pure TiO$_2$). Thus, the capacity of TiO$_2$ anode for NIBs can be increased by carbon coating at a low current rate. However, pure TiO$_2$ seems to have better rate performance than that of TiO$_2$@C, which may be due to the relatively poor rate capability of amorphous carbon.[9,10] TiO$_2$@C-rGO delivers average reversible capacity of 290, 242, 207, 180, and 152 mAh g^{-1} at 0.1, 0.2, 0.5, 1, and 2 Ag^{1-}, respectively. This result suggests that TiO$_2$@C-rGO possesses a very good rate capability and much higher capacity than that of TiO$_2$@C. Therefore, the hybrid nanostructures (TiO$_2$@C-rGO) exhibit not only large capacity, but also enhanced electrochemical kinetics (high rate performance). This result suggests that rGO plays a vital role in electron transfer at high current density, and the presence of rGO is remarkably favorable for enhancing the capacity and rate capability of the electrode material. Figure 5d depicts the cycling performance of the three samples at 0.1 A g^{-1}. The charge capacity of 225, 117, and 102 mAh g^{-1} after 60 cycles could be maintained for TiO$_2$@C-rGO, TiO$_2$@C, and pure TiO$_2$, respectively. This suggests that TiO$_2$@C-rGO displays the best cycling stability among the three samples. In order to test the long-term cycling performance of TiO$_2$@C-rGO, a Na ion half-cell made from TiO$_2$@C-rGO was run at 0.5 A g^{-1} for 1000 cycles, after aging at 0.1 A g^{-1} for 5 cycles. As shown in Figure 5e, TiO$_2$@C-rGO

delivers the reversible (charge) capacity starting at 185 mAh g^{-1} and still maintains at 159 mAh g^{-1} after 1000 cycles at 1 A g^{-1} as well as high Columbic efficiency, indicating excellent cycling stability. It is suggested that the superior electrochemical performance of TiO$_2$@C-rGO could be largely due to the enhanced kinetics arising from the rGO addition and the fast Na ions and electronics transfer between well-dispersed carbon-coated mesoporous TiO$_2$ mesocrystals and conductive graphene network (as depicted in Figure 6a).

In order to verify the electrochemical performance of pure TiO$_2$, TiO$_2$@C, and TiO$_2$@C-rGO electrodes, AC impedance measurements were performed on the fresh batteries made of the three samples in the frequency range from 1 MHz to 100 mHz. As shown in Figure 6b, each Nyquist plot comprises the electrolyte resistance (Rs) at high frequencies, a depressed semicircle at the middle frequencies arising from charge transfer resistance (Rct) and a slope at low frequencies representing the Warburg impedance (W) related to the diffusion process. Obviously, the Rct of TiO$_2$@C (601 Ω) was lower than that of pure TiO$_2$ (753 Ω), but the Rct of TiO$_2$@C-rGO hybrid electrode (230 Ω) was much lower than that of the above two electrodes. The EIS results (Figure S8) from the cells after cycling test (50 cycles at 0.1 A g^{-1}) also confirm this result. Thus, it is verified that TiO$_2$@C-rGO hybrid electrode has the best electronic conductivity. In addition, the Warburg
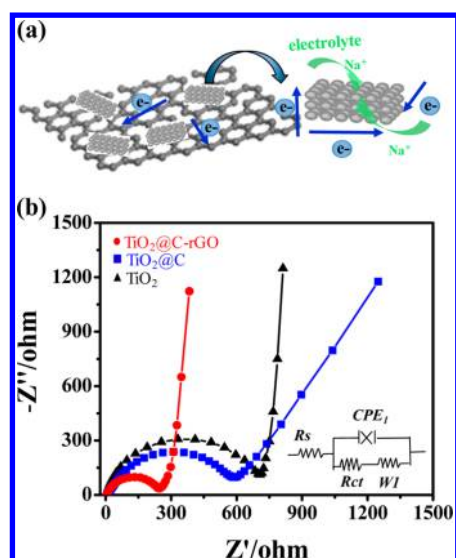
Figure 6. (a) Schematic illustration of transport pathway of Na ion and electrons in TiO$_2$@C-rGO. (b) Electrochemical impedance spectra (EIS) of pure TiO$_2$, TiO$_2$@C, and TiO$_2$@C-rGO. The inset in (b) is the corresponding equivalent circuit.

impedance of TiO$_2$@C electrode is larger than that of the other two electrodes, which may be due to the low Na ion diffusion rate of amorphous carbon. This result is consistent with the rate capability test discussed in the preceding section. The XRD patterns of the cycled electrode at the first discharge and charge are shown in Figure S9. Although the crystallinity of the TiO$_2$ continuously weakens, the anatase structure could be maintained during the discharge and charge process. This result is similar to the previous study.[25,26,28]

4. CONCLUSION

In summary, hybrid nanostructures (TiO$_2$@C-rGO) were successfully synthesized through a facile one-step route including in situ growth of oriented self-assembly of TiO$_2$ mesocrystals on graphene oxide. Such hybrid material possesses a very large surface area (279 m^2 g^{-1}), mesoporous nature, and single-crystal-like structure. It is also revealed that the capacity of TiO$_2$ electrode for NIBs can be improved by carbon coating at a low current rate, but it shows limited capacity at a high current rate. Remarkably, the enhanced electrochemical kinetics and large capacity could be simultaneously achieved by designing the hybrid material. The hybrid nanostructures exhibited a highly reversible capacity of 300 mAh g^{-1} at 100 mA g^{-1} for Na ion storage. Even at a high rate of 2 Ag^{1-}, a reversible capacity of 152 mAh g^{-1} still remained, demonstrating a superior rate capability. It is worth mentioning that a stable capacity of 159 mAh g^{-1} can be maintained after 1000 cycles at 1 A g^{-1}, indicating excellent cycling stability for Na ion storage. It is suggested that the superior electrochemical performance of TiO$_2$@C-rGO could be largely due to the enhanced kinetics arising from the rGO addition and the fast Na ions and electronics transfer between well-dispersed carbon-coated mesoporous TiO$_2$ mesocrystals and conductive graphene network. These results render such hybrid nanostructures a promising material for energy storage and conversion.

AUTHOR INFORMATION

Corresponding Authors
*E-mail: winter0514@163.com.
*E-mail: wei-mingdeng@fzu.edu.cn.
Notes
The authors declare no competing financial interest.

REFERENCES

(1) Armand, M.; Tarascon, J. M. *Nature* **2008**, *451*, 652−657.
(2) Croguennec, L.; Palacin, M. R. *J. Am. Chem. Soc.* **2015**, *137*, 3140−3156.
(3) Tarascon, J.-M. *Nat. Chem.* **2010**, *2*, 510−510.
(4) Pan, H.; Hu, Y.-S.; Chen, L. *Energy Environ. Sci.* **2013**, *6*, 2338−2360.
(5) Kim, Y.; Ha, K.-H.; Oh, S. M.; Lee, K. T. *Chem. - Eur. J.* **2014**, *20*, 11980−11992.
(6) Kang, H.; Liu, Y.; Cao, K.; Zhao, Y.; Jiao, L.; Wang, Y.; Yuan, H. *J. Mater. Chem. A* **2015**, *3*, 17899−17913.
(7) Yabuuchi, N.; Kubota, K.; Dahbi, M.; Komaba, S. *Chem. Rev.* **2014**, *114*, 11636−11682.
(8) Stevens, D. A.; Dahn, J. R. *J. Electrochem. Soc.* **2001**, *148*, A803−A811.
(9) Xu, Y.; Zhu, Y.; Liu, Y.; Wang, C. *Adv. Energy Mater.* **2013**, *3*, 128−133.
(10) Ponrouch, A.; Goñi, A. R.; Palacín, M. R. *Electrochem. Commun.* **2013**, *27*, 85−88.
(11) Hu, Z.; Wang, L.; Zhang, K.; Wang, J.; Cheng, F.; Tao, Z.; Chen, J. *Angew. Chem., Int. Ed.* **2014**, *53*, 12794−12798.
(12) Kim, H.; Hong, J.; Yoon, G.; Kim, H.; Park, K.-Y.; Park, M.-S.; Yoon, W.-S.; Kang, K. *Energy Environ. Sci.* **2015**, *8*, 2963−2969.
(13) Liu, Y.; Xu, Y.; Zhu, Y.; Culver, J. N.; Lundgren, C. A.; Xu, K.; Wang, C. *ACS Nano* **2013**, *7*, 3627−3634.
(14) Liang, L.; Xu, Y.; Wang, C.; Wen, L.; Fang, Y.; Mi, Y.; Zhou, M.; Zhao, H.; Lei, Y. *Energy Environ. Sci.* **2015**, *8*, 2954−2962.
(15) Wang, L.; Zhang, K.; Hu, Z.; Duan, W.; Cheng, F.; Chen, J. *Nano Res.* **2014**, *7*, 199−208.
(16) Jian, Z.; Liu, P.; Li, F.; Chen, M.; Zhou, H. *J. Mater. Chem. A* **2014**, *2*, 13805−13809.
(17) Zhu, C.; Mu, X.; van Aken, P. A.; Yu, Y.; Maier, J. *Angew. Chem., Int. Ed.* **2014**, *53*, 2152−2156.
(18) Senguttuvan, P.; Rousse, G.; Seznec, V.; Tarascon, J.-M.; Palacín, M. R. *Chem. Mater.* **2011**, *23*, 4109−4111.
(19) Wang, W.; Yu, C.; Lin, Z.; Hou, J.; Zhu, H.; Jiao, S. *Nanoscale* **2013**, *5*, 594−599.
(20) Fu, S.; Ni, J.; Xu, Y.; Zhang, Q.; Li, L. *Nano Lett.* **2016**, *16*, 4544−4551.

(21) Wu, D.; Li, X.; Xu, B.; Twu, N.; Liu, L.; Ceder, G. *Energy Environ. Sci.* **2015**, *8*, 195−202.

(22) Xu, Y.; Memarzadeh Lotfabad, E.; Wang, H.; Farbod, B.; Xu, Z.; Kohandehghan, A.; Mitlin, D. *Chem. Commun.* **2013**, *49*, 8973−8975.

(23) Cha, H. A.; Jeong, H. M.; Kang, J. K. *J. Mater. Chem. A* **2014**, *2*, 5182−5186.

(24) Qin, G.; Zhang, X.; Wang, C. *J. Mater. Chem. A* **2014**, *2*, 12449−12458.

(25) Kim, K.-T.; Ali, G.; Chung, K. Y.; Yoon, C. S.; Yashiro, H.; Sun, Y.-K.; Lu, J.; Amine, K.; Myung, S.-T. *Nano Lett.* **2014**, *14*, 416−422.

(26) Yang, Y.; Ji, X.; Jing, M.; Hou, H.; Zhu, Y.; Fang, L.; Yang, X.; Chen, Q.; Banks, C. E. *J. Mater. Chem. A* **2015**, *3*, 5648−5655.

(27) Wu, L.; Bresser, D.; Buchholz, D.; Giffin, G. A.; Castro, C. R.; Ochel, A.; Passerini, S. *Adv. Energy Mater.* **2015**, *5*, 1401142.

(28) Hong, Z.; Zhou, K.; Huang, Z.; Wei, M. *Sci. Rep.* **2015**, *5*, 11960.

(29) Hong, Z.; Zhou, K.; Zhang, J.; Huang, Z.; Wei, M. *J. Mater. Chem. A* **2015**, *3*, 17412−17416.

(30) Su, D.; Dou, S.; Wang, G. *Chem. Mater.* **2015**, *27*, 6022−6029.

(31) Chen, C.; Wen, Y.; Hu, X.; Ji, X.; Yan, M.; Mai, L.; Hu, P.; Shan, B.; Huang, Y. *Nat. Commun.* **2015**, *6*, 6929.

(32) Hong, Z.; Wei, M. *J. Mater. Chem. A* **2013**, *1*, 4403−4414.

(33) Uchaker, E.; Cao, G. *Nano Today* **2014**, *9*, 499−524.

(34) Hong, Z.; Wei, M.; Lan, T.; Jiang, L.; Cao, G. *Energy Environ. Sci.* **2012**, *5*, 5408−5413.

(35) Song, R. Q.; Cölfen, H. *Adv. Mater.* **2010**, *22*, 1301−1330.

(36) Fattakhova-Rohlfing, D.; Zaleska, A.; Bein, T. *Chem. Rev.* **2014**, *114*, 9487−9558.

(37) Tahir, M. N.; Oschmann, B.; Buchholz, D.; Dou, X.; Lieberwirth, I.; Panthöfer, M.; et al. *Adv. Energy Mater.* **2016**, *6*, 1501489.

(38) Deng, S.; Berry, V. *Mater. Today* **2016**, *19*, 197−212.

(39) Chen, K.; Song, S.; Liu, F.; Xue, D. *Chem. Soc. Rev.* **2015**, *44*, 6230−6257.

(40) Liu, H.; Cao, K.; Xu, X.; Jiao, L.; Wang, Y.; Yuan, H. *ACS Appl. Mater. Interfaces* **2015**, *7*, 11239−11245.

(41) Lan, T.; Qiu, H.; Xie, F.; Yang, J.; Wei, M. *Sci. Rep.* **2015**, *5*, 8498.

(42) Dresselhaus, M. S.; Jorio, A.; Hofmann, M.; Dresselhaus, G.; Saito, R. *Nano Lett.* **2010**, *10*, 751−758.

(43) Chen, D.; Wang, G.-S.; He, S.; Liu, J.; Guo, L.; Cao, M.-S. *J. Mater. Chem. A* **2013**, *1*, 5996−6003.

(44) Pan, L.; Zhao, H.; Shen, W.; Dong, X.; Xu, J. *J. Mater. Chem. A* **2013**, *1*, 7159−7166.